Radio Science, Volume ???, Number , Pages 1?? ,

Radar Interference Blanking in Radio Astronomy using a Kalman Tracker

W. Dong

Department of Electrical and Computer Engineering, Brigham Young University, Provo, UT, USA

B. D. Jeffs

Department of Electrical and Computer Engineering, Brigham Young University, Provo, UT, USA

J. R. Fisher

National Radio Astronomy Observatory, Green Bank Observatory, WV, USA

Radio astronomical observations of highly Doppler shifted spectral lines of neutral hydrogen and the hydroxyl molecule must often be made at frequencies allocated to pulsed air surveillance radar in the 1215-1350 MHz frequency range. The Green Bank telescope (GBT) and many other observatories must deal with these terrestrial signals. Even when strong radar fixed clutter echoes are removed, there are still weaker aircraft echoes present which can corrupt the data. We present an algorithm which improves aircraft echo blanking using a Kalman filter tracker to follow the path of a sequence of echoes observed on successive radar antenna sweeps. Aircraft tracks can be used to predict regions (in azimuth and range) for the next expected echoes, even before they are detected. This data can then be blanked in real time without waiting for the pulse peak to arrive. Additionally, we briefly suggest an approach for a new Bayesian algorithm which combines tracker and pulse detector operations to enable more sensitive weak pulse detection. Examples are presented for Kalman tracking and radar transmission blanking using real observations at the GBT.

1. Introduction

The frequency bands of spectral line emissions of neutral hydrogen (1420.4 MHz) and the hydroxyl molecule (1612.2, 1665.4, 1667.4, and 1720.5 MHz) from cosmic sources are protected by international spectrum allocations, but observed radiation from very distant objects is Doppler shifted to much lower frequencies due to the expansion of the universe. Some of this radiation is shifted into the 1215-1350 MHz frequency range allocated to radar transmissions, such as from the ARSR-3 air surveillance system. These radar signals can overwhelm astronomical observations, and have been reported to be a significant problem at the Green Bank Telescope (GBT) (see *Zhang et al.* [2003], *Fisher* [2001a] and *Fisher* [2001b]), Arecibo (see *Ellingson and Hampson* [2003] and *Ellingson and Hampson* [2002]) and other observatories. However, the radar signal is impulsive and transient, so for radio astronomy observation, one solution is to "time-blank" by simply not including radar corrupted data samples during spectrum estimation (*Ravier and Weber* [2000] *Zhang et al.* [2003]). Time blanking has also been used to mitigate the effect of transmissions from mobile wireless communications services (see *Leshem and v.d. Veen* [1999] *Boonstra et al.* [2000] *Leshem et al.* [1999]). Additionally, a non-blanking approach to radar RFI mitigation has been proposed where detected pulses are removed by parametric signal subtraction without discarding data (*Ellingson and Hampson* [2002]).

To illustrate the problem addressed in this paper, Figures 1 and 2 present some 1292 MHz data recorded at the GBT which clearly shows the radar signal. A detailed description and analysis of this real-world data is provided in *Fisher* [2001a] and *Fisher* [2001b]. This ARSR-3 radar system is located in Bedford VA, about 104 km from the GBT. The rotating transmit antenna completes a full 360 degree sweep in 12 seconds, with a pulse repetition

0048-6604/05/$11.00

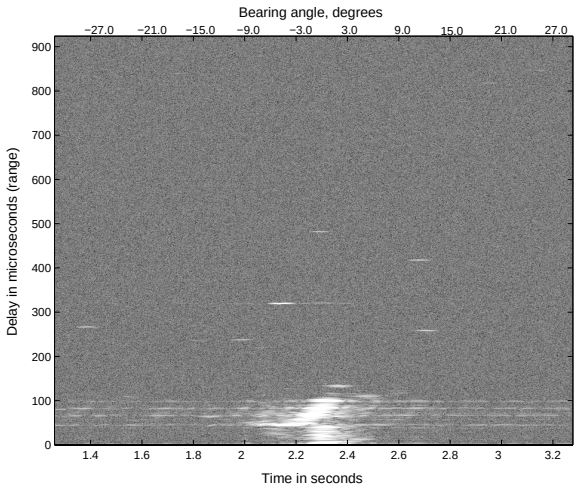

Figure 2. Typical radar sweep time frame as seen at the GBT. Data are presented in range-azimuth (or equivalently range-bearing) map form, with intensity corresponding to echo signal power. Zero degrees corresponds to the transmitter beam passing overhead at the GBT.

interval of approximately 2.93 ms and pulse length of 3.5 μs.

Figure 1 shows pulse intensity as a function of delay relative to the first arriving path for a single transmitted pulse. Strong signal terms can be seen out to a delay of 135 microseconds, most of which are due to reflections from the hilly terrain around the GBT (i.e. ground clutter). These can typically be excised using fixed time window blanking. The group of echo returns at 430 microseconds is from an aircraft, and blanking it is more problematical since it is not present at this same location during each successive transmit antenna sweep.

Figure 2 gives a two dimensional view of the data known as a range-azimuth map. The 1-D time series data has been broken into window blocks and re-ordered so that each transmit pulse, with its associated echoes, is plotted as a one pixel wide column in the map. Each column thus contains a 2.93 ms window of received data. The vertical axis represents time between the first detected arrival for a pulse and its longer delayed echoes. Since the transmit antenna is rotating, the coarse time horizontal axis can be interpreted as corresponding to angle (azimuth) of the transmit antenna pointing direction. A 60 degree segment of the full sweep is shown, centered on the time when the transmit beam passes overhead at the GBT. Again two types of radar signals are seen. Bright regions in the range of 0 to 120 μs are fixed echoes from nearby mountainous terrain. Bright points at longer delay times are aircraft echoes. Note the wide transmit antenna sidelobe pattern for the echo at 310 μs delay.

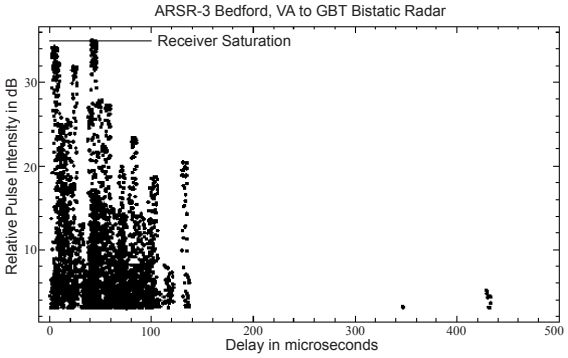

Figure 1. Pulse intensity as a function of delay from the directly arriving pulse

1.1. Approach

There are two basic approaches to blanking which we will call respectively, "time window blanking" (TWB) and "detected pulse blanking" (DPB). Strong direct-path pulses and nearby fixed terrain clutter echoes have a predictable repetition cycle and can be removed by simple TWB. In this approach a fixed set of time intervals, synchronized to the radar pulse repetition rate, are removed from the data during each transmit antenna sweep cycle. All data between the first arrival time and a fixed delay (of for example 135 μs) is removed for each transmit pulse, eliminating ground clutter echoes and their associated sidelobe structure. TWB is considered the baseline minimum level of radar RFI blanking, and is performed on all data sets presented in the remainder of this paper. Its effect on the signal seen in Figure 2 would be to remove all data in the horizontal band between 0 and 135 μs of delay.

On the other hand, aircraft echoes arrive at arbitrary times due to aircraft motion, and thus must be detected before they can be blanked. DPB is used in this case to remove a window of data in the range-azimuth map surrounding each detected aircraft echo, including transmit antenna beampattern sidelobes which span many transmit pulses.

Two difficulties arise with DPB:

1. It is very hard to perform blanking in real time because aircraft echoes include wide sidelobe patterns from the radar transmit beampattern which extend over tens of degrees before and after the central peak and over several range bins due to the transmit pulse length (see Figure 2). For real-time operation the echo must be anticipated and the full beam sidelobe and pulselength structure must be removed before and after the echo peak arrives.

2. Echoes weak enough to make detection of even the peak amplitude difficult may still cause significant corruption to the data set. This is because astronomical signals of interest are typically tens of decibels below the noise floor.

This paper presents a Kalman filter tracker for aircraft echo motion which can be used to resolve both problems. The proposed method utilizes time-history information across multiple past radar antenna sweeps to predict detection locations in the next upcoming antenna pass. The first problem (real-time blanking) is solved by forming a prediction region around an anticipated echo peak to guide data removal for each affected transmit pulse. We designate this algorithm the "Kalman Detected Pulse Blanker" (KDPB).

In a fully digital radio telescope implementation it would be possible to perform real-time blanking without KDPB; you could blank pulses stored in memory as they are detected. However, this requires sufficient memory to handle several seconds of data latency, and enough computational capacity to keep up with echo detection and tracking while also performing the desired scientific analysis. The long latency requirement arises from transmit beampattern sidelobes which can precede the detectable central echo peak by several seconds (see Figure 2).

We propose the alternate solution illustrated in Figure 3. The detection, tracking, and blanking window functions run in parallel with the original signal processing path. Using track history information it is possible to predict the next pulse arrival and form a blanking window in advance. This architecture has several advantages over a non-predictive "blank after detection" approach.

1. This blanking system may be added to an existing telescope signal path with minimum disruption of the current analytical instrumentation or software.

2. It can be applied to both analog or digital instrumentation because the sampled, digitized data used for pulse detection and tracking need not be used for downstream science analysis. The only required system output is the blanking (on – off) control signal.

3. No signal path latency is introduced.

4. Digital sample rates need only support the radar pulse bandwidth. The analytical signal path may be broader band, but detection processing requires only about a 2 MHz sample rate.

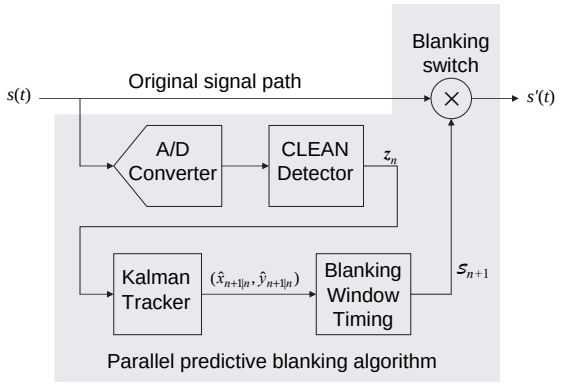

Figure 3. Processing architecture for predictive real-time blanking. The original instrumentation signal path is interrupted only by insertion of a blanking switch and tapping of a signal to feed the pulse detector.

This paper will focus on the Kalman tracker based KDPB solution to the first (i.e. real-time blanking) problem cited above. Its use on real radar transmission data recorded at the GBT will be demonstrated. However, we note that the developed track history can also be used to form a prior probability distribution for pulse arrivals. This distribution can be used in a Bayesian framework to improve weak echo detection and thus solve the second problem with DPB mentioned above. An improved detection scheme called "Bayesian-Kalman Detected Pulse Blanking" (BKDPB) will be briefly introduced as another application for the tracker. The detection theoretic basis for, and performance analysis of BKDPB will be fully developed in a following paper.

1.2. Data Preprocessing

Before echo pulse tracking can be accomplished there are a number of data preprocessing steps which must be performed. Details are beyond the scope of this space-limited paper (see *Dong* [2004]), but the basic operations are listed here for orientation:

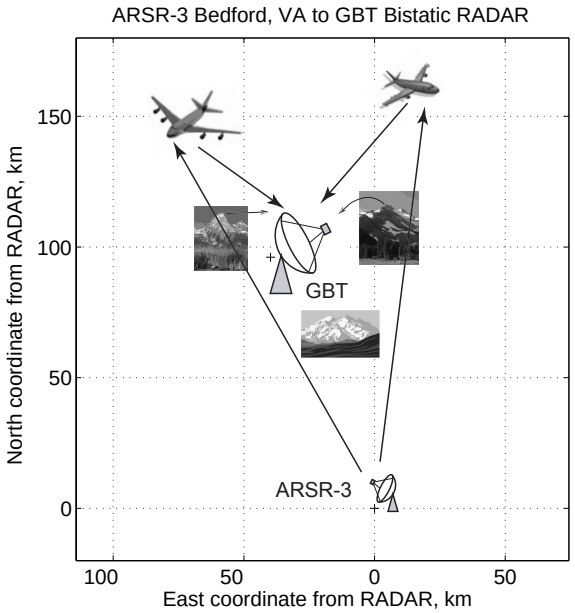

Figure 4. Bistatic geometry of radar signal seen at the GBT. Echoes from nearby mountains are strong, and have fixed timing relative to the antenna sweep. Aircraft echoes are non-stationary.

1. Data acquisition was accomplished by sampling a 10 MHz band from the GBT 1.15-1.17 GHz receivers at 20 Msamp/sec. The specifics for the data sets used here are described in *Fisher* [2001a] and *Fisher* [2001b].

2. A full digital radar receiver was implemented for optimal pulse detection with unknown time of arrival, amplitude, and phase. Processing included complex baseband band shifting, band select filtering, matched filtering (matched to the transmitted pulse shape), and complex envelope detection.

3. Data was reformatted into time range and azimuth bins with synchronization to transmit pulse interval timing. This required careful first arrival pulse detection and was necessary in order to form range-azimuth map data presentation for echo position tracking. This process is fairly complex due to irregular pulse repetition periods and because the receiver and transmitter are non cooperating processes.

4. TWB was applied to blank the first 135 μs of every pulse to remove clutter from nearby terrain features.

5. The large extent of an echo in range and azimuth dimensions can cause many pixels for a single pulse to exceed the detection threshold. All these threshold crossings from a single aircraft must be grouped and represented by a single detection centroid point. This was accomplished with a modified version of the CLEAN algorithm (*Högbom* [1974]) which also permits discrimination of distinct echoes whose sidelobe patterns overlap.

2. Kalman Tracking for Interfering Aircraft Echoes

This section presents tracker implementation details. A classical Kalman filter approach as often used for radar target following (see for example *K.V.Ramachandra* [2000], *Zarchan and Musoff* [2000], and *Mahafza* [2000]) was used with some modifications specific to the radio astronomy RFI scenario. State equations for aircraft dynamics are represented in Cartesian, $x-y$, coordinates and are thus non-linearly related to the natural polar (range and azimuth) coordinate system of the radar detector. This mismatch necessitates use of an extended Kalman filter implementation to linearize the observation data points.

Also, in the RFI case we have a "bistatic" radar scenario where the transmitter and receiver are widely separated. The ARSR-3 signals seen at the GBT originate at a transmitter site approximately 104 km south-southeast of the GBT, as shown in Figure 4. This geometry complicates estimating true physical range and azimuth relative to the GBT. Azimuth in all discussions to follow is taken to be relative to the transmitter location, with zero degrees referenced to when the transmit beam passes directly overhead at the GBT. On the other hand, range is measured as the two–way bistatic pulse echo travel time from radar transmitter to the GBT, and is not directly proportional to actual distance of the aircraft from either the transmitter or the GBT alone. However, since the goal is not to precisely localize each aircraft in real-world coordinates, but to build a predictive tracker in any suitable coordinate system, we make no attempt to estimate actual range relative to the GBT. Using the bistatic "pseudo range" measurement does not affect tracker performance unless the (unknown) observed azimuth angle from the GBT to the aircraft is changing rapidly. Tracker computations, including the dynamical motion model, will treat the bistatic pseudo range as an actual geometric range.

The CLEAN algorithm provides isolated detections in range and azimuth, $\boldsymbol{z}_n = [r_n, \theta_n]^T$, for each

radar antenna sweep. These detections serve as inputs to the tracker. Here n is the antenna sweep, "snapshot" index for time t_n. Also for notational simplicity in this discussion we focus on detections from a single track. The desired tracker outputs at snapshot n are a prediction point, $(\hat{x}_{n+1|n}, \hat{y}_{n+1|n})$, where the next detection is expected, and shape parameters for an elliptical uncertainty region, $\mathcal{S}_{n+1}$, centered on this point (see Figure 5). The size of $\mathcal{S}_{n+1}$ depends on the quality of the track, and gets larger with an increase in observation noise, missed snapshot detections, or rapid acceleration of the target. $\mathcal{S}_{n+1}$ selects the region for predictive real-time blanking, or the region of increased prior probability for an arriving echo pulse for the detection step in snapshot $n+1$.

2.1. Dynamic and Observation Models

The tracker employs a position-and-velocity state space model to describe dynamics of motion for the aircraft. Constant velocity motion perturbed by a correlated–in–time zero mean Gaussian random process acceleration vector, $\boldsymbol{a}_n$, is assumed. Measurements are obtained at discrete sample "snapshot" times, t_n, separated by intervals of T seconds. The dynamic motion model is

$$\begin{aligned} \boldsymbol{x}_{n+1} &= \boldsymbol{F}\boldsymbol{x}_n + \boldsymbol{G}\boldsymbol{a}_n, \text{ where} \\ \boldsymbol{x}_n &= \begin{bmatrix} x_n & y_n & \dot{x}_n & \dot{y}_n \end{bmatrix}^T, \\ \boldsymbol{F} &= \begin{bmatrix} 1 & 0 & T & 0 \\ 0 & 1 & 0 & T \\ 0 & 0 & 1 & 0 \\ 0 & 0 & 0 & 1 \end{bmatrix}, \\ \boldsymbol{G} &= \begin{bmatrix} \frac{T^2}{2} & 0 & T & 0 \\ 0 & \frac{T^2}{2} & 0 & T \end{bmatrix}^T. \end{aligned} \tag{1}$$

$\boldsymbol{x}_n$ is the state vector for a single aircraft, and x_n and $\dot{x}_n$ represent position and velocity respectively in the x direction, $\boldsymbol{F}$ is the state transition matrix, and $\boldsymbol{G}$ is the input distribution matrix used to properly update the state vector in response to acceleration. $\boldsymbol{a}_n = [a_{x,n}, a_{y,n}]^T$ is the acceleration vector at time snapshot n. Acceleration is viewed as the unknown driving input process to the system modeled by the state equations. In the absence of acceleration, the state is updated each snapshot to increment positions consistent with constant velocity motion.

The measurement model relates polar observations, $\boldsymbol{z}_n$, to the state equation coordinates and includes observation measurement noise:

$$\begin{aligned} \boldsymbol{z}_n &= \boldsymbol{h}(\boldsymbol{x}_n) + \boldsymbol{v}_n, \text{ where} \\ \boldsymbol{h}(\boldsymbol{x}_n) &= \begin{bmatrix} \sqrt{x_n^2 + y_n^2} \\ \tan^{-1} \frac{y_n}{x_n} \end{bmatrix}, \\ \boldsymbol{v}_n &= [v_{r,n}, v_{\theta,n}]^T, \end{aligned} \tag{2}$$

r_n and θ_n are the measured range and azimuth respectively at snapshot n, with corresponding measurement noise $v_{r,n}$ and $v_{\theta,n}$.

2.2. Kalman Prediction Equations

Given echo detections and associated track history up to snapshot n, the first step in a Kalman filter iteration is to predict the next state vector and update the prediction error covariance estimate as follows:

$$\hat{\boldsymbol{x}}_{n+1|n} = \boldsymbol{F}\hat{\boldsymbol{x}}_{n|n}, \tag{3}$$

$$\boldsymbol{P}_{n+1|n} = \boldsymbol{F}\boldsymbol{P}_{n|n}\boldsymbol{F}^T + \boldsymbol{G}\boldsymbol{Q}\boldsymbol{G}^T, \tag{4}$$

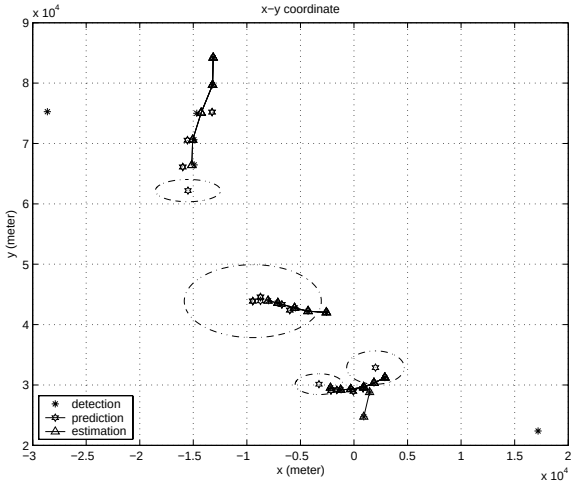

Figure 5. An example of Kalman tracking performance for data acquired at the GBT. Four aircraft tracks have been automatically established and plotted, including a pair of crossing tracks. Data from five snapshots is shown spanning approximately 24 seconds. The final point plotted for each track is the prediction point, $(\hat{x}_{n+1|n}, \hat{y}_{n+1|n})$. Prediction regions, $\mathcal{S}_{n+1}$, shown by the dashed ellipses vary in size according to track quality. Note that the center track has a large $\mathcal{S}_{n+1}$ due to a missed detection. Predictive real-time blanking is accomplished by excising the prediction region data.

where

$$\begin{aligned}
\hat{\boldsymbol{x}}_{n|n} &= \text{filtered state estimate at } t_n \\
&\quad \text{given data through } t_n, \\
\boldsymbol{P}_{n|n} &= \text{filtered state error covariance}, \\
\hat{\boldsymbol{x}}_{n+1|n} &= \text{predicted state estimate}, \\
\boldsymbol{P}_{n+1|n} &= \text{predicted state error covariance}, \\
\boldsymbol{Q} &= \text{acceleration covariance}.
\end{aligned}$$

$\hat{\boldsymbol{x}}_{n|n}$ and $\boldsymbol{P}_{n|n}$ are computed using filter equations, (5)–(7), presented in Section 2.3. Note that the prediction point, $(\hat{x}_{n+1|n}, \hat{y}_{n+1|n})$, is given by the first two elements of $\hat{\boldsymbol{x}}_{n+1|n}$. We define the elliptical region, $\mathcal{S}_{n+1}$ to be centered on this point and to have radii r_x and r_y proportional to $\sqrt{[\boldsymbol{P}_{n+1|n}]_{1,1}}$ and $\sqrt{[\boldsymbol{P}_{n+1|n}]_{1,1}}$ respectively. Thus the larger the prediction error variance, the larger $\mathcal{S}_{n+1}$ grows to represent our uncertainty as to where the next radar echo will be detected.

Figure 5 illustrates this behavior. The plot shows track evolution for real GBT data over five snapshots for a dense scene with multiple, overlapping aircraft tracks. The ellipses show prediction regions, $\mathcal{S}_6$, for each established track. Note the variety of sizes corresponding to variations in track quality. For real-time processing these prediction regions are blanked for the next expected echoes, even before they are detected. In the BKDPB Bayesian scheme the prior information that detections are more likely inside these ellipses is used for a combined tracking-with-detection algorithm to improve sensitivity to weak pulses.

2.3. Kalman Update (Filter) Equations

When a new snapshot of detections, $\boldsymbol{z}_{n+1}$, from CLEAN is available, the Kalman update step completes the iteration begun with equations (3) and (4) as follows:

$$\begin{aligned}
\hat{\boldsymbol{x}}_{n+1|n+1} &= \hat{\boldsymbol{x}}_{n+1|n} + \boldsymbol{K}_{n+1} \\
&\quad \times \left[\boldsymbol{z}_{n+1} - \boldsymbol{h}\left(\hat{\boldsymbol{x}}_{n+1|n} \right) \right], \qquad (5) \\
\boldsymbol{P}_{n+1|n+1} &= \left[\boldsymbol{I} - \boldsymbol{K}_{n+1} \boldsymbol{H}_{n+1} \right] \\
&\quad \times \boldsymbol{P}_{n+1|n} \qquad (6) \\
\boldsymbol{K}_{n+1} &= \boldsymbol{P}_{n+1|n} \boldsymbol{H}_{n+1}^T \qquad (7) \\
&\quad \times \left[\boldsymbol{H}_{n+1} \boldsymbol{P}_{n+1|n} \boldsymbol{H}_{n+1}^T + \boldsymbol{R} \right]^{-1},
\end{aligned}$$

where the extended Kalman filter linearization about t_{n+1} is provided by

$$\begin{aligned}
\boldsymbol{H}_{n+1} &= \left[\frac{\partial h}{\partial \boldsymbol{x}} \right]_{\boldsymbol{x} = \hat{\boldsymbol{x}}_{n+1|n}} \qquad (8) \\
&= \left(\frac{1}{\sqrt{x_{n+1|n}^2 + y_{n+1|n}^2}} \right) \\
&\quad \times \begin{bmatrix} x_{n+1|n} & y_{n+1|n} & 0 & 0 \\ -y_{n+1|n} & x_{n+1|n} & 0 & 0 \end{bmatrix},
\end{aligned}$$

and where $\boldsymbol{K}_{n+1}$ is the Kalman gain matrix.

Range estimation error standard deviation is proportional to the pulse length. Azimuth error deviation is proportional to antenna beamwidth and is statistically independent of range error. Thus range and azimuth measurement error are properly modeled with a measurement error covariance of the simple form

$$\boldsymbol{R} = \begin{bmatrix} \sigma_r^2 & 0 \\ 0 & \sigma_\theta^2 \end{bmatrix}, \qquad (9)$$

where there are no cross correlation terms and variances are constant with respect to range and azimuth. We note that measurement error (noise) modeled in the (x, y) domain would not have this simple structure, would be correlated between x and y, and would be a function of r. However, with the extended Kalman filter approach the above update equations take care of this transformation and the proper correlated structure is found in error covariance matrices $\boldsymbol{P}_{n+1|n+1}$ and $\boldsymbol{P}_{n+1|n}$. After computing (5), (6), and (7), index n is incremented to complete the iteration which started with prediction equations (3) and (4).

2.4. Track Initialization and Management

The prediction and update equations include several parameters that are either assumed known and must be estimated externally (i.e. $\boldsymbol{Q}$ and $\boldsymbol{R}$), or are iteratively estimated but need good initial values for stable track start up ($\boldsymbol{P}_{n|n}$ and $\hat{\boldsymbol{x}}_{n|n}$). Also, in practical multiple target automatic tracking applications it is necessary to deal with a number of ambiguities when interpreting the pulse detection data. We have developed a set of rule–based procedures (more fully described in *Dong* [2004]) to address these issues. The following list describes our approach for initializing and managing tracks.

1. *State Parameter Initialization.* Two successive associated pulse detections are required before a track can be initiated. $\hat{\boldsymbol{x}}_{0|0}$ is initialized with the position of the second detection, and a two-sample

velocity estimate is computed from the position difference between the detections.

To find a practical initialization for $\boldsymbol{P}_{0|0}$, we ran the tracker on synthetic detection data which simulated the aircraft motion seen in real GBT data. After a large number of Monte Carlo random trials, $\boldsymbol{P}_{n|n}$ converged on average to $\boldsymbol{P}_{\infty|\infty} \approx (2 \times 10^3)\boldsymbol{I}$. This value was used to initialize $\boldsymbol{P}_{0|0}$ when processing real data from the GBT.

2. *Constant Parameter Estimates.* The acceleration process covariance is modeled as a constant matrix of the form

$$\boldsymbol{Q} = E\{\boldsymbol{a}_n \boldsymbol{a}_n^T\} = \begin{bmatrix} \sigma_x^2 & \sigma_{xy}^2 \\ \sigma_{xy}^2 & \sigma_y^2 \end{bmatrix}. \tag{10}$$

Values of $\sigma_x^2 = \sigma_y^2 = 12.0$ and $\sigma_{xy}^2 = \sigma_{yx}^2 = 0$ were used in the results described below and were established by qualitative analysis of flight paths in the real GBT data. Parameters were set so that synthetically generated tracks in random trials by the state space model had acceleration rates (turn radii) comparable to what was observed in the real aircraft detection data. $\boldsymbol{a}_n$ was generated by lowpass filtering two mutually independent Gaussian white noise time sequences (one each for $a_x(n)$ and $a_x(n)$). A filter cutoff frequency of $f_c = \frac{1}{100T}$ produced smooth simulated aircraft turning maneuvers which were qualitatively consistent with real track paths seen in the GBT data.

Tracking performance did not appear in practice to be critically dependent on the values set for σ_x^2 and σ_y^2. However, settings significantly higher (by a factor of two or more) increase the size of the prediction region, $\mathcal{S}_{n+1}$ and thus increases likelihood of associating a new detection with the wrong track. Setting these terms too small results in tracks failing to associate the new detection with a track when there has been some maneuver, or direction change.

For initializing $\boldsymbol{R}$ we note that σ_r^2 is proportional to both the receiver noise variance and the square of the transmit pulse length. σ_θ^2 is proportional to noise and to the square of transmit antenna angular rotation rate divided by transmit pulse repetition rate. We have estimated these parameters empirically for the GBT data and treat them as constants in the Kalman update.

3. *Track Association.* For each new snapshot the CLEAN algorithm produces a set of detections. Each of these must be classified as being a newly detected aircraft for which a track must be created, or as belonging to an existing track. Detections which lie within a fixed distance, d_a, from an existing track's prediction point, $(\hat{x}_{n+1|n}, \hat{y}_{n+1|n})$, are associated with that track. To avoid ambiguities, detections which satisfy this criterion for two or more distinct tracks are assigned to the track whose prediction point is closest.

4. *Track Creation.* New detections which are not within a distance d_a of any existing prediction point are designated candidate starting points. The track is created if in the succeeding snapshot, $n+1$, a detection within distance d_n of the candidate point is found which is not associated with any existing track. d_a serves as a bound on how much prediction error is to be tolerated and is proportional to the maximum radius of $\mathcal{S}_{n+1}$. d_n is a bound on the maximum distance an aircraft can travel in T seconds, and is typically much larger than d_a since prediction points are expected to be close to the true location. Since no velocity or direction information is available from a single candidate point, there will be no prediction point at time $n+1$, and the candidate track must accept any unassociated detection within a radius of d_n from the initial detection.

5. *Missed Detections.* If in a given snapshot no new detection is associated with a particular track, it is assumed that the aircraft is still present, but that the detection was missed due to random variation in echo amplitude. Consider missing k successive detections for a given track. In this case, Kalman prediction equations (1), (3), and (4) from prior snapshot, t_{n-k}, are recomputed as a multi–step prediction by replacing T with kT. This produces the desired k–step prediction point $(\hat{x}_{n+1|n-k}, \hat{y}_{n+1|n-k})$ but the prediction error covariance, $\boldsymbol{P}_{n+1|n-k}$, increases and the size of $\mathcal{S}_{n+1}$ grows as compared to a normal single step prediction.

6. *Track Dropping.* A track which has no associated detections in three successive snapshots is terminated.

7. *Track Splitting.* If two or more new detections are associated with a single track then the track is split into separate tracks for each new detection. These split tracks have a common history for $t \leq t_{n-1}$ but for $t \geq t_n$ are computed as distinct tracks. This scenario arises when aircraft paths cross or when a new aircraft detection occurs close to an existing track prediction point of a different aircraft.

3. A Combined Kalman Tracker and Bayesian Detector

In a conventional radar detector, all range-azimuth bins are assumed to be equally likely to contain an echo. Detections are made when the magnitude–squared matched filter output exceeds a predetermined constant threshold, τ. Thresholds are set to yield a specified probability of false alarm (PFA). For a fixed PFA, the probability of detection (PD) is a function of the receiver design and signal statistics, such as signal to noise ratio.

In the context of the Kalman tracker, one need not assume all bins have the same probability of detection. The track histories provide prior information which indicates a higher probability of echoes being detected in prediction regions, $\mathcal{S}_{n+1}$. We propose a Bayesian detection scheme where a spatially dependent prior probability density function for the presence of an echo, $f(x, y)$, is computed using the $\mathcal{S}_{n+1}$ ellipses to designate areas of increased density. With this approach it is possible to increase the overall PD without an increase in PFA. A detailed theoretical development of this detector is found in *Dong* [2004] and in a forthcoming paper. When used for RFI removal we refer to the method as Bayesian-Kalman Detected Pulse Blanking (BKDPB).

Here it is simply noted in summary that with a rigorous detection theoretic development it can be shown that the net effect of the Bayesian detector is to make the detection threshold, $\tau(x, y)$, spatially varying, with local minima at the prediction point centroids of the $\mathcal{S}_{n+1}$ regions, as illustrated in Figure 8. Section 4 presents a comparison of spectral density estimates with conventional DPB and the proposed BKDPB. The new method produces less radar pulse bias in the spectral estimate.

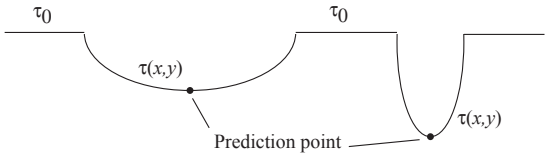

Figure 8. The threshold τ is determined by the prior distribution $f(x, y)$ of the presence of a pulse. τ_0 is the constant threshold outside the elliptical regions, $\mathcal{S}_{n+1}$. $\tau(x, y)$ is at a local minimum corresponding to each prediction point. The two concavities represent decreased threshold according to the prior probability inside two different sized $\mathcal{S}_{n+1}$.

4. Experimental Results

Two sets of real data recorded at the GBT for a 10 MHz wide band around 1292 MHz were used to test the echo detection algorithm, tracking, and blanking performance. Set one was collected in April of 2002, and set two in January of 2003.

Figure 6 presents a typical Kalman tracking result for data set one. This example illustrates successfully tracking 11 aircraft, including crossing tracks and track splitting. A number of other detections are seen which have not yet been associated with tracks. Conventional fixed threshold detection was used here. Throughout this entire data set, the track prediction regions formed good estimates of the next echo location, and were suitable for real-time predictive blanking (KDPB).

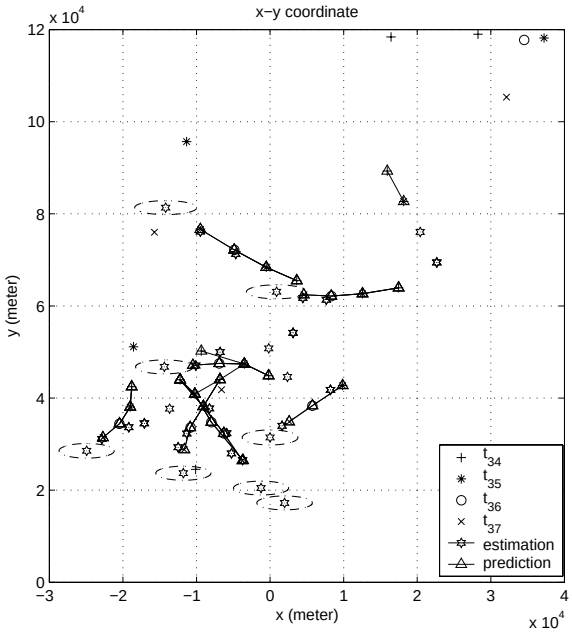

Figure 6. Tracking result example for five antenna sweep snapshots, t_34 to t_38. Note that not ever sweep was used, so the snapshot interval, T, in this case is 60 seconds. Ellipses indicate prediction regions for the final snapshot.

Figure 7 illustrates effectiveness of the real-time blanking technique (KDPB). Though processing was

actually performed on recorded data set two, blanking regions were based (as they would be for real-time operation) on the Kalman tracker predictions using only past history data. This data set includes 50 radar antenna rotations. All blanking was implemented by "zero-stuffing" , that is, placing zeros into the time samples where radar transmissions are detected (*Zhang et al.* [2003]). The lower curve shows that the power spectrum after KDPB is dramatically improved, with lower bias due to radar aircraft echo contamination.

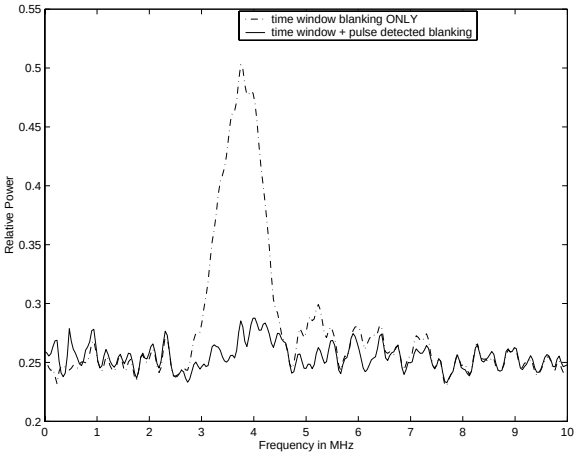

Figure 7. Power spectrum estimates for two approaches to radar pulse blanking. Only TWB was used for the upper curve. Both TWB and KDPB were used for the lower curve. The 1292 MHz radar pulse carrier frequency has been mixed down to about 4 MHz in this plot.

Figure 9 illustrates how the Bayesian-Kalman detector in BKDPB can find weaker echoes that would be missed with conventional constant threshold detection. These tracks come from data set one and were computed using BKDPB. The three echoes marked by rectangles were not detected when the same data was processed with KDPB.

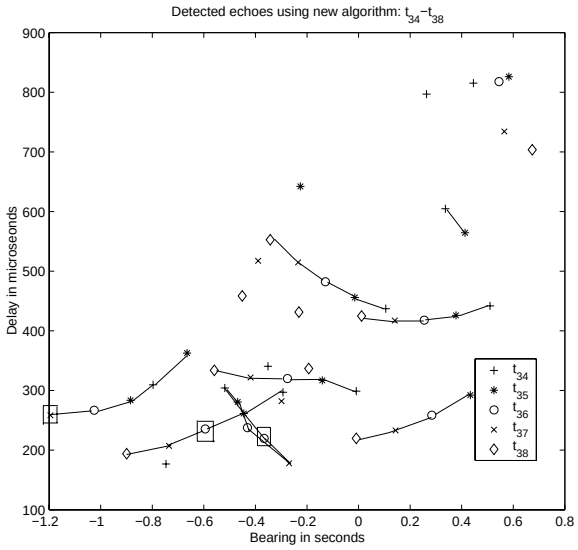

Figure 9. Real data detection results for both algorithms for five snapshots from the GBT. Note that 3 weaker pulses (inside the rectangles) are missed by the constant threshold algorithm (DPB), and picked up with BKDPB detection.

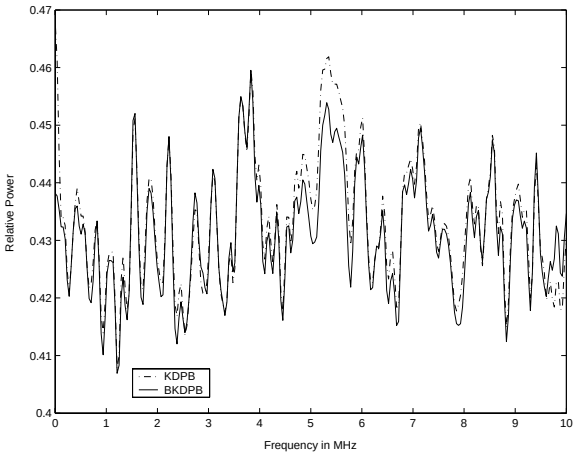

Figure 10. Power spectrum estimate for a segment of data set two containing two weak echoes. The constant threshold detection of KDPB was used for the upper curve, but no echoes were found. In the lower curve the Bayesian-Kalman detector in BKDPB located and blanked three echoes and thus reduced radar bias near 5.5 MHz.

Figure 10 shows the differnece between spectral estimates computed using the KDPB and BKDPB blanking algorithms. In this particular data window from data set two there were no strong aircraft echoes so KDPB made no detections. There are two weak aircraft echoes which were detected with BKDPB and the corresponding time samples were blanked (set to zero) when computing a power spectrum. The resulting curve shows reduced bias near 5.5 MHz corresponding to the radar pulse center frequency. The larger deviations at 0 and 10 MHz are not fully understood, but are assumed to be band edge effects.

5. Conclusions

Detected pulse blanking using Kalman filter tracking techniques has been shown to be an effective approach for real-time radar RFI mitigation. Bias due to radar pulses in GBT observations was reduced as compared to to simple fixed time window blanking (TWB). Also, the new Bayesian combined tracking and detection algorithm has been shown to improve blanking of weak aircraft echo pulses, leading to a further reduction in bias in power spectrum estimates of the noise floor (see Figures 7 and 10). Multiple simultaneous tracks were managed (as many as 11) for aircraft seen in real observations at the GBT. Crossing tracks, congested traffic regions, and intermittent track detections were all handled satisfactorily. The computational load for the tracker is modest since it operates on detections only and is updated only at the transmit antenna sweep rate. We have run the tracking portion of the code in MATLAB faster than real time using a modest PC. However, the required digital radar receiver and pulse detector operate at the raw baseband signal sample rate and require a significant digital signal processing platform, though such systems are widely in use. This paper presented the system development and analyzed performance by post processing previously recorded data. A next step is to implement this in a true real-time environment on our experimental RFI mitigation DSP test platform. This will permit us to evaluate the true impact this system can have on improve radio astronomical observation science.

Acknowledgments. This work is supported by the National Science Foundation grant number AST-9987339.

References

Boonstra, A., A. Leshem, A.-J. van der Veen, A. Kokkeler, and G. Schoonderbeek (2000), The effect of blanking of tdma interference on radio-astronomical observations: experimental results, in *Proc. of the IEEE International Conf. on Acoust,, Speech, and Signal Processing*, vol. 6, pp. 3546–3549.

Dong, W. (2004), Time blanking for gbt data with radar rfi, Master's thesis, Brigham Young University.

Ellingson, S., and G. Hampson (2002), Rfi and asynchronous pulse blanking in the 1230-1375 mhz band at arecibo, *Tech. rep.*, Ohio State University.

Ellingson, S., and G. Hampson (2003), Mitigation of radar interfernece in l-band radio astronomy, *The Astrophysical Journal Suplement Series*, *147*, 167–176.

Fisher, J. (2001a), Summary of rfi data samples at green bank, *Tech. rep.*, National Radio Astronomy Observatory, Green Bank Observatory.

Fisher, J. (2001b), Analysis of radar data from february 6, 2001, *Tech. rep.*, National Radio Astronomy Observatory, Green Bank Observatory.

K.V.Ramachandra (2000), *Kalman Filtering Techniques for Radar Tracking*, Marcel Dekker.

Leshem, A., and A.-J. v.d. Veen (1999), Introduction to interference mitigation techniques in radio astronomy, in *Perspectives in Radio Astronomy, Technologies for Large Antenna Arrays*, edited by A. Smolders and M. van Haarlem, NFRA, Dwingeloo, The Netherlands.

Leshem, A., A.-J. v.d. Veen, and E. Deprettere (1999), Detection and blanking of gsm interference in radio-astronomical observations, in *Proceedings of the 2nd IEEE Workshop on Signal Processing Advances in Wireless Communications*, pp. 374–377.

Mahafza, B. (2000), *Radar Systems Analysis and Design Using MATLAB*, Chapman and Hall/CRC Press.

Högbom, J. (1974), Aperture synthesis with a nonregular distribution of interferometer baselines, *Astronomy and Astrophysics Supplement*, *15*, 417.

Ravier, P., and R. Weber (2000), Robustness in rfi detection for time-blanking, *Tech. rep.*, LESI and ESPEO, University of Orlans, France.

Zarchan, P., and H. Musoff (2000), Fundamentals of kalman filtering: A practical approach, *Progressin Astronautics and Aeronautics*, *190*, 257–291.

Zhang, Q., Y. Zheng, S. Wilson, J. Fisher, and R. Bradley (2003), Combating pulsed radar interference in radio astronomy, *The Astronomical Journal*, *126*, 1588–1594.

W. Dong and B. D. Jeffs, Department of Electrical and Computer Engineering, Brigham Young University, Provo, UT 84602, USA (wzhdong@hotmail.com, bjeffs@ee.byu.edu)

J. R. Fisher, National Radio Astronomy Observatory, P.O. Box 2, Green Bank, WV 24944, USA (rfisher@nrao.edu)

(Received _____.)